



Unveiling enhanced electron-mediated peroxymonosulfate activation for degradation of emerging organic pollutants

Junjie Xu^a, Yanchi Yao^a, Chao Zhu^a, Lun Lu^b, Qile Fang^c, Zhiqiao He^a, Shuang Song^a, Baoliang Chen^d, Yi Shen^{a,*}

^a Key Laboratory of Microbial Technology for Industrial Pollution Control of Zhejiang Province, College of Environment, Zhejiang University of Technology, Hangzhou 310032, China

^b State Environmental Protection Key Laboratory of Environmental Pollution Health Risk Assessment, South China Institute of Environmental Sciences, Ministry of Ecology and Environment, Guangzhou 510655, China

^c Advanced Institute of Natural Sciences, Beijing Normal University at Zhuhai, Zhuhai 519087, China

^d Department of Environmental Science, Zhejiang University, Hangzhou 310058, China

ARTICLE INFO

Keywords:

Peroxymonosulfate activation
Electronic coupling
Energy barrier optimization
Nano-island catalyst
Emerging organic pollutant

ABSTRACT

The electron transfer pathway activated by peroxymonosulfate (PMS) has garnered significant attention for the removal of emerging organic pollutants from water. However, overcoming the two-step energy barriers involved in electron transport across reaction interfaces presents a formidable challenge. To surmount the two-step energy barriers of pollutant-catalyst and catalyst-PMS, a catalyst with nano-island structure was developed, forming efficient ternary catalytic interfaces with PMS and pollutants. The presence of atomic pairs within the catalyst punched through the electron transport channels, resulting in a pseudo-first-order kinetic rate of 2.06 min^{-1} for bisphenol A, which was 5.1 times higher than that of the control sample. The electronic coupling of atomic pairs exerted a profound impact on the splitting of d-orbitals, effectively elevating the d-orbital unoccupancy and reducing the two-step energy barriers encountered by electrons from pollutants to catalysts, and subsequently to PMS, which promoted efficient degradation of pollutants. Furthermore, through the association of two-step energy barrier, the feasibility of utilizing the orbital interaction as a descriptor of the degradation rate by electron-mediated PMS activation was demonstrated. Additionally, the intermediates generated through electron transfer pathway exhibited a lower risk of bioaccumulation. This work inspires insights into the electron-mediated mechanism of multinary catalytic interface reactions.

1. Introduction

Emerging organic pollutants in water environments pose significant risks to aquatic organisms and humans due to their high biotoxicity and recalcitrant biodegradability [1–4]. In the pursuit of efficient removal of detrimental pollutants, researchers have extensively explored the activation of peroxymonosulfate (PMS) as a promising method for eliminating emerging organic pollutants in water [5–7]. Among various reaction pathways, the electron transfer pathway has gained attention due to its stability against the presence of concurrent organic and inorganic compounds in the environment, providing exceptional anti-interference capabilities [8,9]. In this pathway, electrons from adsorbed pollutants are transported through the catalyst to PMS, establishing electron transport channels (ETCs) on the constructed

ternary catalytic interfaces [10,11]. However, the availability of efficient ternary catalytic interfaces is predominantly influenced by the nanomorphology and adsorption strength of catalyst [12,13]. Significantly, the efficiency of ETCs relies heavily on the energy barrier of electron transport including the electron abstracted (from pollutants) and transport (to PMS) ability of catalyst [11,14]. Consequently, the effectiveness of pollutant degradation via electron transfer pathway is principally governed by the intrinsic properties of catalyst, implying that based on efficient ternary catalytic interfaces constructed through reliable catalysts, it is promising to facilitate efficient ETCs by curtailing the energy barriers to ultimately expedite the electron transfer pathway.

In recent years, an emerging class of single-atom catalysts known as nano-islands has gained considerable attention [15]. These nano-islands confine individual atoms within metals or metal compounds, and their

* Corresponding author.

E-mail address: shenyi@zjut.edu.cn (Y. Shen).

<https://doi.org/10.1016/j.apcatb.2023.123356>

Received 11 August 2023; Received in revised form 24 September 2023; Accepted 29 September 2023

Available online 1 October 2023

0926-3373/© 2023 Elsevier B.V. All rights reserved.

protruding "island" nanomorphology and exceptional surface reactivity facilitate the adsorption of PMS and pollutants, thereby promoting the formation of ternary catalytic interfaces [16]. Compared to carbon materials, nano-islands exhibit a dense distribution of energy states near the Fermi level, resulting in an increased abundance of readily accessible electrons [17,18]. These distinctive attributes foster efficient electron transport and establish the nano-island as an ideal platform for expediting electron transfer pathway. Although there is a lack of specific reports on the application of nano-islands in PMS activation, its superiority has been acknowledged in other investigations involving interfacial adsorption process and intrinsic electron transport [19]. Hence, the utilization of nano-islands holds great promise for electron-mediated PMS activation. Nevertheless, the hindrances faced by electron transfer pathway, both at the initiation points (extraction from pollutants) and termination points (transport to PMS), play a crucial role in impeding the flow of electron transport. Thence, further investigation is warranted to explore the potential of modifying nano-islands as a means to reduce the energy barriers and boost electron transport.

In the realm of single-atom catalyst, atomic paired catalyst as a novel design approach, exhibits an electronic coupling between adjacent bimetallic atoms [20]. The electronic coupling allows for the modulation of electronic structure, endowing the catalyst with the capability to adjust electron capture and adsorption strength, which builds the initiation points of ETCs up [21]. Simultaneously, by effectively complexing the atomic pairs with PMS, it is anticipated that the channel can be expanded, facilitating the establishment of terminal points in ETCs [22]. Specifically, the asymmetrical charge distribution of atomic pairs can influence the bond length and adsorption configuration of adsorbates, augmenting their propensity for fine-tuning adsorption strength and electron-capture/release [23–25]. Consequently, the incorporation of electronic coupling into nano-islands holds promise for electron-capture/release to reduce the two-step energy barriers. Nonetheless, while the electronic coupling in atomic pairs has been preliminarily explored, the underlying mechanisms responsible for its intrinsic enhancement in PMS activation remain uninvestigated.

In this study, an atomic paired nano-island structure was obtained by calcination of metal-organic frameworks doped Co and Fe (Co-Fe-MDNI). In the elucidation of interfacial behaviors of PMS and pollutants, the Co-Fe-MDNI/PMS* complexes, resulting from the combination of the catalyst and PMS, displayed a strong pollutant adsorption capability, leading to the formation of ternary catalytic interfaces and achieving a pseudo-first-order kinetic rate of 2.06 min^{-1} for BPA, which was 5.1 times higher than the control sample. Through in situ characterization and density functional theory (DFT) calculation, it was discovered that the remarkable capability of enhanced electron transfer pathway relied on the punching through of ETCs at the ternary catalytic interfaces. The underlying mechanism was further elucidated that the electronic coupling of atomic pairs induced the reduction of d-orbital splitting energy, lowering the two-step energy barriers of pollutant-catalyst and catalyst-PMS, thus efficiently expediting the degradation of pollutants. Meanwhile, the plausible degradation pathways of BPA were proposed based on the identified intermediate products and Fukui indices, and electron transfer pathway was found to be low risk in terms of bioaccumulation compared to alternative pathways.

2. Experimental section

2.1. Materials and reagents

All chemical reagents were analytical grade and used without further purification. 2-Aminoterephthalic acid was purchased from Sigma-Aldrich and titanium isopropoxide was purchased from Macklin Biochemical Co., Ltd. Iron (III) acetylacetonate, cobalt (II) acetylacetonate, N, N-Dimethylformamide (DMF, 99.9 %) and methanol (MeOH, 99.9 %) were provided by Sinopharm Chemical Reagent Co., Ltd. Analytical reagents of carbamazepine (CBZ), 2,2',4,4'-tetrahydroxybenzophenone

(BP-2), sodium dihydrogen phosphate and dibasic sodium phosphate were obtained from J&K, Shanghai. Bisphenol A (BPA), sulfamethoxazole (SMX), tert-butyl alcohol (TBA), p-benzoquinone (p-BQ), L-histidine (L-h), dimethyl sulfoxide (DMSO) and potassium dichromate were obtained from Aladdin, Shanghai.

2.2. Synthesis of catalysts with nano-islands

In a typical procedure, $\text{NH}_2\text{-MIL-125}$ was synthesized by a one-pot hydrothermal procedure according to the reported method. Titanium isopropoxide was dissolved in DMF and methanol followed by ultrasound treatment for 5 min. Then, 2-Aminoterephthalic acid was added to the solution under stirring and incubated. Subsequently, the mixture was transferred into a 100 mL Teflon-lined stainless-steel autoclave and heated in the oven. After cooling to room temperature, the mixture was centrifuged and washed with DMF and MeOH. After drying under vacuum, the obtained powder was dispersed in MeOH with cobalt acetylacetonate and iron acetylacetonate for 12 h. The powder was filtered and dried in a vacuum drying oven. Finally, the dried powder was calcined in a tubular furnace and without any treatment. The obtained samples were metal-organic framework (MOF) derived nano-islands, thus named as Co-Fe-MDNI, Co-MDNI and Fe-MDNI according to the metal sources added. The sample without metal sources was named MOF derived carbon skeleton (MDC). Details are presented in [Supporting Information](#).

2.3. Characterization

Physical structures of MDC, Co-MDNI, Fe-MDNI and Co-Fe-MDNI were investigated using field emission scanning electron microscope (FESEM), high-resolution transmission electron microscopy (HR-TEM), Brunauer-Emmett-Teller (BET) surface areas and aberration-corrected high-angle annular dark field scanning transmission electron microscopy (AC-HAADF-STEM). The chemical structures were investigated using synchrotron X-ray absorption spectroscopy (XAS), Fourier transform infrared spectroscopy (FTIR), X-ray diffraction (XRD), X-ray photoelectron spectroscopy (XPS) and in situ Raman spectrometry. The contents of metal and the intermediate products of pollutant degradation were determined by inductively coupled plasma-mass spectrometry (ICP-MS) and liquid chromatograph mass spectrometer (LC-MS), respectively. The electrochemical properties were determined using open circuit potential (OCP) and cyclic voltammetry (CV) tests. Details are presented in [Supporting Information](#).

2.4. Pollutants degradation procedure

Pollutants degradation was conducted in a typical reaction system, which Co-Fe-MDNI (0.1 g/L) was added into a reactor filled with 100 mL of a solution containing 10 mg/L of BPA and 1.0 mM of phosphate buffer solution (PBS), following by the addition of 20 mg PMS to initiate the oxidation reaction. During the reaction, 1 mL of solution was quickly sampled from the reactor and filtered through a $0.22 \mu\text{m}$ film at given time intervals, in which 0.5 mL methanol was pre-injected to quench the excess free radicals for further analysis. The solution was analyzed using a Waters 2695 high performance liquid chromatography (HPLC) equipped with a fluorescence detector. In experiments with different variables, specific amounts of catalyst and PMS were added into the solution, and pH was adjusted before the reaction. In order to assess the contribution of different radicals in BPA degradation, 10 mM of TBA ($\cdot\text{OH}$), MeOH ($\cdot\text{OH}$ and $\text{SO}_4^{\cdot-}$), p-BQ ($\cdot\text{O}_2$), L-h ($^1\text{O}_2$), DMSO (high-valent metal oxides) and $\text{K}_2\text{Cr}_2\text{O}_7$ (electron) were added to scavenge specific reactive species, respectively. All the tests were performed in duplicate. The analytical conditions of intermediates detection by LC-MS were as follows: the mobile phase with a flow rate of 0.3 mL min^{-1} started with 30/70 (v/v) 0.1 % formic acid solution/methanol, kept for 15 min. Details are presented in [Supporting Information](#).

3. Results and discussion

3.1. Designs and characterization of nano-islands with atomic pairs

As illustrated in Fig. 1a, the metal sources, Co and Fe, were encapsulated within the channels of MOF through the coordination of metal ions with $-NH_2$ functional groups present in the organic linkers. Subsequent thermal treatment led to the conversion of the metal centers into TiO_2 , which became anchored to the original carbon-skeleton. The resulting atomic pairs were uniformly embedded in the TiO_2 lattice, resembling atomic pairs trapped on nano-islands. During the calcination, the abundant pore structures formed in MDC, Co-MDNI, Fe-MDNI, and Co-Fe-MDNI provided materials with large specific surface areas (Fig. S1, Table S1), which were determined by N_2 adsorption/desorption tests to be 361.27, 261.54, 245.36, and 203.76 m^2/g , respectively. These large specific surface areas might extend the exposure of active sites and

bolster the adsorption of PMS and pollutants [26]. The formation of nano-islands was confirmed by FESEM and HR-TEM techniques (Fig. S2-S7). The FESEM image (Fig. 1b) showed densely anchored TiO_2 nanoparticles on the carbon skeleton, resembling a distributed archipelago, which could intensify the dispersion of active sites and improve the utilization of atoms. The HR-TEM image (Fig. 1c) displayed continuous lattice fringes with interplanar spacings of 0.324 and 0.347 nm, corresponding to the (110) planes of rutile TiO_2 and (101) planes of anatase TiO_2 , respectively [27–29]. Moreover, a slight variation in lattice distances was observed in the dark region I (0.324 nm) and bright region II (0.328 nm) of Co-Fe-MDNI (Fig. 1d), possibly attributed to the segregation of Co-Fe dopants in TiO_2 crystals, deriving from the transformation of the crystal field. The uniform distribution of Co, Fe, and Ti elements on the carbon skeleton without noticeable aggregation in Fig. 1e.

Furthermore, based on the findings from ICP-MS analysis (Table S2),

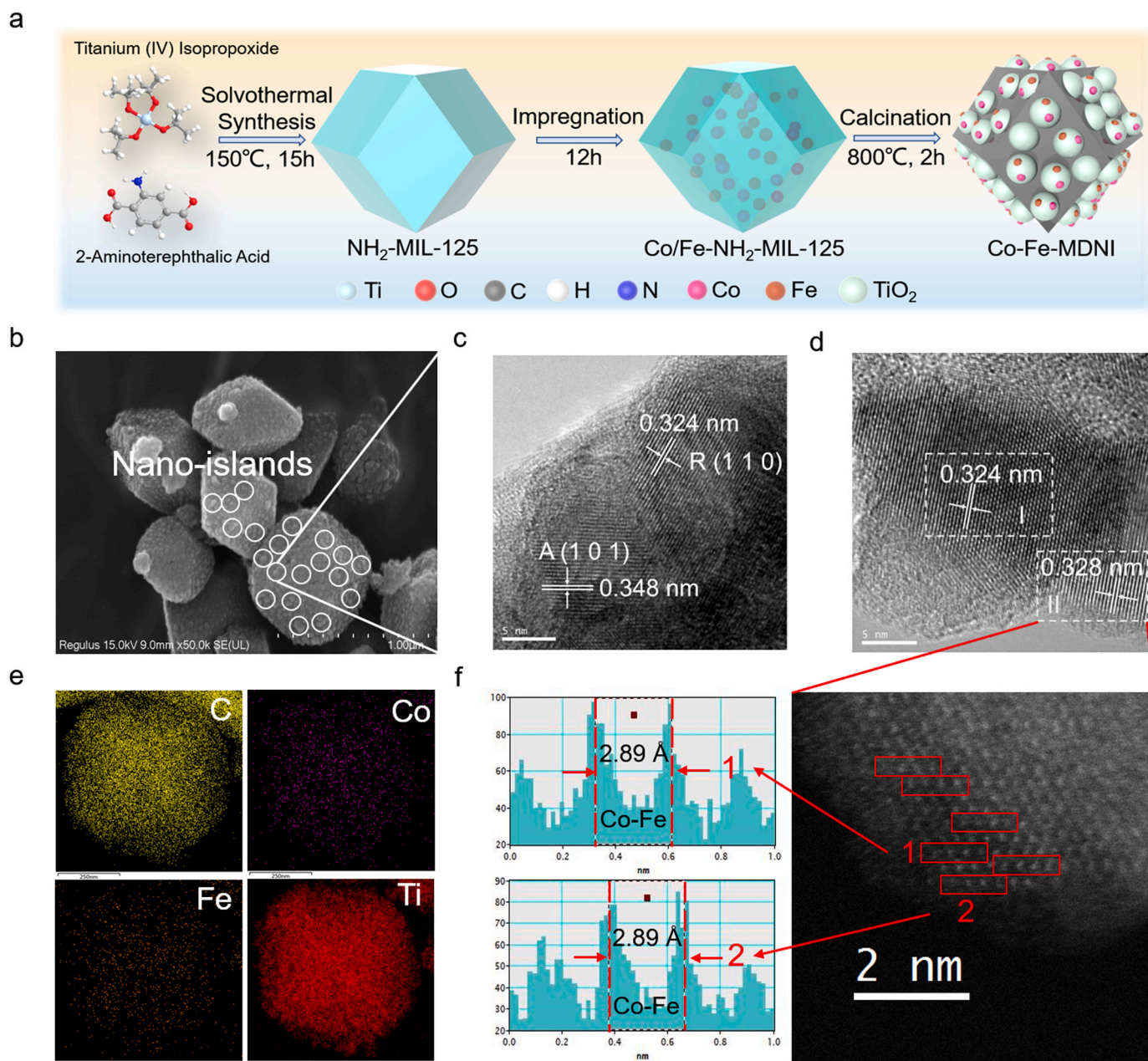


Fig. 1. a) The synthesis process of Co-Fe-MDNI. b) FESEM, c, d) HR-TEM, and e) EDS mapping images of Co-Fe-MDNI. f) AC-HAADF-STEM image of Co-Fe-MDNI and corresponding intensity profiles of adjacent Co and Fe atoms.

the contents of Co and Fe in Co-Fe-MDNI were determined to be 2.34 % and 0.17 %, respectively, which might be attributed to the greater tendency of Co to coordinate with N atoms, facilitating the formation of a single-atom structure. In FTIR spectra patterns, the peaks of C-N, C=O, C-OH, and Ti-O-Ti without Co-N or Fe-N observed could verify the existence of carbon-skeleton without Co or Fe, indicating that the carbon skeleton and TiO₂ complemented each other (Fig. S8) [30–33]. The combination of ICP-MS and FTIR results inferred that Co and Fe elements were doped into the nano-island structure. XPS was employed to

verify the presence of Co-Fe atoms embedded in the TiO₂ lattice and confirm the nano-island structure. Co and Fe atoms were incorporated into the TiO₂ lattice, exhibiting higher brightness than the adjacent Ti atoms, with a measured distance of approximately 2.89 Å (Fig. 1f). Electron energy loss spectroscopy (EELS) results (Fig. S9) further confirmed the presence of Fe and Co atomic pairs. The doping of Co-Fe atomic pairs has a significant effect on the lattice parameters of TiO₂, as reflected in the XRD patterns (Fig. S10). In the patterns, prominent crystal planes of anatase (101) and rutile (110) were clearly discernible,

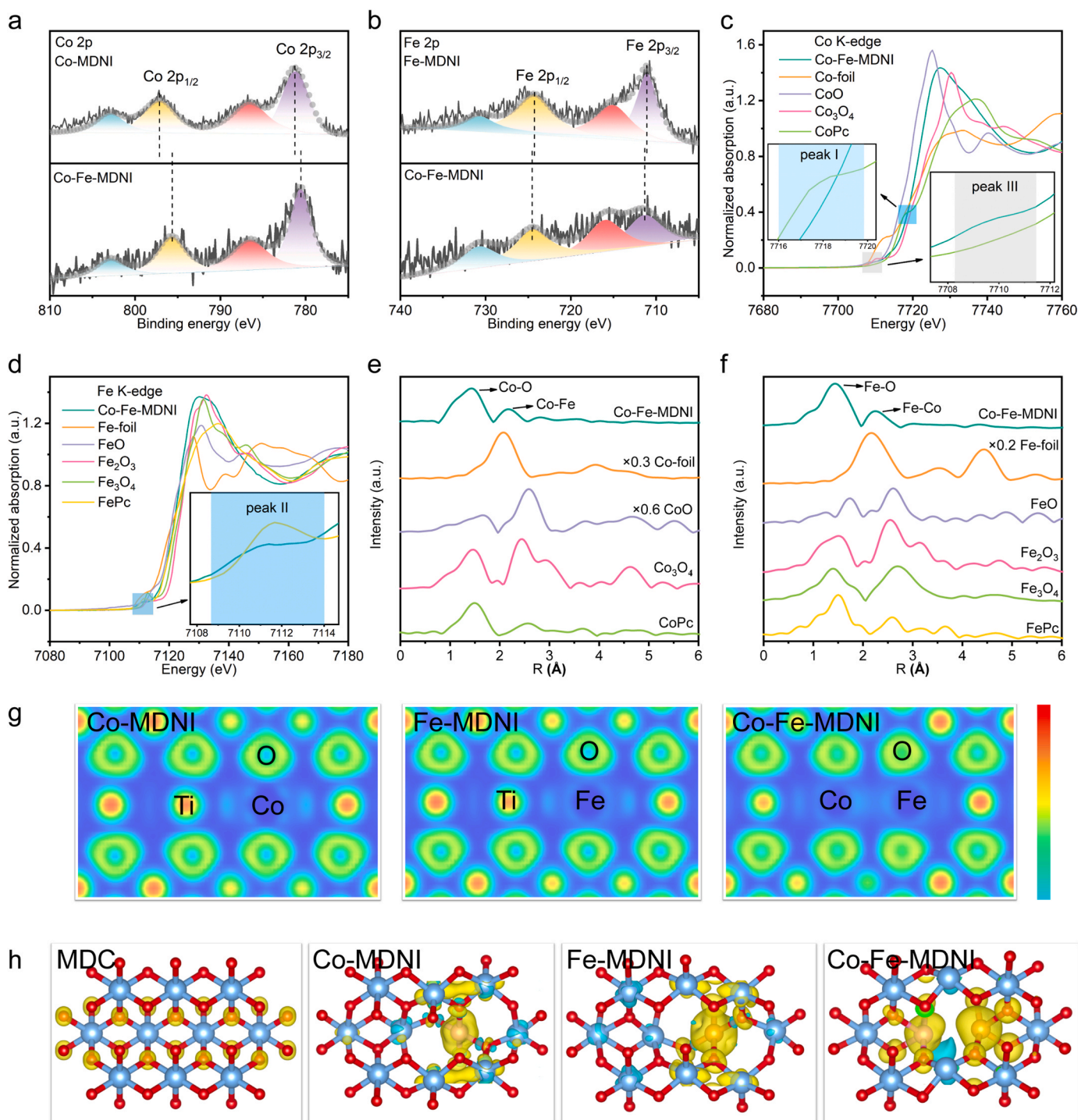


Fig. 2. XPS spectra of Co-Fe-MDNI for a) Co 2p and b) Fe 2p regions. c) Co and d) Fe K-edge XANES spectra of Co-Fe-MDNI and references. e) Co and f) Fe K-edge EXAFS spectra of Co-Fe-MDNI and references. g) Electron localization functions of Co-MDNI, Fe-MDNI and Co-Fe-MDNI. h) Spin density distribution of MDC, Co-MDNI, Fe-MDNI, and Co-Fe-MDNI.

which were consistent with the observation by HR-TEM. However, no discernible oxide-related peaks corresponding to Co or Fe were evident, substantiating the presence of nano-island structure from a lateral perspective. The refinement of the XRD pattern revealed an increase in the lattice parameters (*a*, *c*) and an elongation of the Ti-O bond length [34], which might be ascribed to the incorporation of Co-Fe atomic pairs (Table S3). Combined with previous AC-HAADF-STEM image and EELS results, it can be inferred that with the state of isolated Co-Fe atomic pairs, Co and Fe have been successfully incorporated into the TiO₂ crystal lattice, leading to an expansion of the unit cell and formation of the nano-island structure.

To analyze the chemical composition and preliminarily assess the electronic states of Co-Fe-MDNI, XPS was employed (Fig. S11-S12) [35–37]. The Co and Fe 2p XPS spectra (Fig. 2a–b) were examined to determine the oxidation states of Co and Fe. In the Co 2p region of Co-Fe-MDNI, Co 2p_{3/2} (781.0 eV) and Co 2p_{1/2} (796.6 eV) subpeaks were observed, along with two satellite peaks at 786.6 and 802.95 eV. Notably, the binding energies of Co 2p_{3/2} and Co 2p_{1/2} peaks of Co-Fe-MDNI were higher than those of Co-MDNI by 0.2 and 0.3 eV, respectively. Moreover, the binding energies of Fe 2p_{3/2} and Fe 2p_{1/2} peaks of Co-Fe-MDNI shifted to lower energies about 0.3 and 0.5 eV compared to those of Fe-MDNI. Additionally, the projected density of states (PDOS) of Co and Fe matched well in Co-Fe-MDNI (Fig. S13). These observations indicate strong electronic coupling between adjacent Co and Fe atoms, suggesting that the electronic structure can be regulated in Co-Fe-MDNI.

X-ray absorption spectroscopy was employed to analyze the Co-Fe-MDNI, providing insights into the coordination of metal atoms and an in-depth understanding of electronic structure. The X-ray absorption near-edge structure (XANES) spectra of Co K-edge and Fe K-edge are presented in Fig. 2c–d. Notably, the Co-Fe-MDNI exhibited distinct coordination environments, evident from the dissimilar peak shapes and intensities in Co and Fe K-edge XANES spectra compared to the standard CoPc and FePc with typical Co-N₄ and Fe-N₄ structures [38,39]. The amplified peaks I and II depicted in the figures exhibited a discernible and intensified integrated front edge peak intensity in Co-Fe-MDNI in contrast to CoPc and FePc, which signified that the electronic structure of Co-Fe-MDNI was modulated due to the 3d hybridization of Co and Fe atoms [40,41]. The decline or rise of pre-peak feature signifies the depletion or growth of the coordination configuration, respectively, providing information of hybrid orbitals in the absorbing atoms and coordination atoms [42]. The reduced intensity in peaks I and II of Co-Fe-MDNI, compared to CoPc and FePc, further supported the distortion of symmetry induced by the electronic coupling of Co-Fe atomic pairs, resulting in shakedown transitions (1 s → 4p_z) in the original peak of CoPc and FePc with a square planar configuration [43,44]. The emergence of fine structure in pre-peak region (peak III) was attributed to the dipole-forbidden 1 s to 3d transition that was allowed by the 3d-4p orbital mixing resulting from the disrupted centrosymmetric environment [42]. These observations validate a modification in the coordination environment, indicating changes in the d-orbitals of Co and Fe that can be attributed to the electronic coupling. To investigate the coordination of Co and Fe atoms in Co-Fe-MDNI, Fourier-transformed extended X-ray absorption fine structure (FT-EXAFS) analysis was conducted. The dominant peak at 1–2 Å was due to the first coordinated shell of Co-O bond, excluding the presence of metallic Co and various Co oxides (Fig. 2e), which suggested that Co element existed in the Co-Fe-MDNI catalyst in the form of coordination with O, and the Co-Fe bond at 2.67 Å confirmed the existence of Co-Fe atomic pairs. Quantitative analysis showed that the coordination numbers of Co-O and Co-Fe path were approximately 4 and 1, respectively (Table S4). The second coordination shell with low intensity was attributed to the single scattering path of Fe-Co (Fig. 2f). The extracted interatomic distance of Fe-Co (2.72 Å) was approximately consistent with that of Co-Fe (2.67 Å), and the coordination number value (≈1.0) verified that most Fe ions were successfully bonded with Co to generate the Co-Fe

hetero-atomic moiety (Table S4). Moreover, wavelet-transform plots of Co-Fe-MDNI were distinguished from the reference samples (Fig. S14–15). Hence, it can be inferred that the electronic coupling of Co-Fe leads to the variation in electronic structure, particularly in the d-orbitals.

To gain further insight into the effect of electronic coupling on the d-orbitals, models of MDC, Co-MDNI, Fe-MDNI, and Co-Fe-MDNI were constructed for DFT calculations (Fig. S16). Analysis of the electronic localization functions (ELF, Fig. 2g) revealed significant distorted electronic symmetry in Co-MDNI, Fe-MDNI, and Co-Fe-MDNI due to the incorporation of Co and Fe atoms. Furthermore, the Co and Fe sites exhibited a high degree of electron delocalization, implying that the electronic coupling bolsters the efficient transport of free electrons in Co-Fe-MDNI, which played a crucial role in the ETCs. Meanwhile, electronic spin density distributions (Fig. 2h) showed that Co-Fe-MDNI had significant electronic spin polarization compared to Co-MDNI and Fe-MDNI, which might be attributed to the production of more unpaired electrons. The increased unpaired electrons produced by Co-Fe atomic pairs suggest a variation in d-orbital energy level due to the strong electronic coupling according to the molecular orbital theory [45]. Furthermore, the states of electronic spin polarization were consistent with the magnetic moments of each material. Table S5 displayed that the spin moment of MDC (0 μ_B), Co-MDNI (0.36 μ_B), Fe-MDNI (2.87 μ_B), and Co-Fe-MDNI (7.00 μ_B) elevated as Co and Fe atoms incorporated. These findings imply that the unpaired electrons in d-orbitals are significantly affected by electronic coupling, leading to an increased d-orbital unoccupancy, which may have a favorable effect on the PMS activation by Co-Fe-MDNI for pollutant degradation.

3.2. Construction of ternary catalytic interfaces

Following an understanding of the inherent electronic characteristics, the degradation experiments were conducted using the emerging organic pollutant BPA as a probe to investigate the electron-mediated PMS activation. The rates of pollutant degradation for Co-MDNI and Fe-MDNI were found to be 3.8 and 2.9 times that of MDC, respectively. However, Co-Fe-MDNI exhibited the strongest pollutant removal capacity, with a pseudo-first-order rate constant (*k*_{obs}) up to 2.06 min^{−1}, which was 5.1 times than that of MDC (Fig. 3a, Table S6). Compared to recently advanced materials, Co-Fe-MDNI exhibited significantly superior removal efficiency (Fig. 3b). The origin of enhanced efficiency including the interfacial reactions and intrinsic mechanisms would be investigated.

Concerning the establishment of ternary catalytic interfaces, a comprehensive study was conducted involving in situ studies and density functional theory (DFT) calculations. In the in situ Raman spectra patterns (Fig. 3c), a peak at 827 cm^{−1} was observed, which could be attributed to the formation of Co-Fe-MDNI/PMS*. This peak was absent in the spectra of both PMS and Co-Fe-MDNI, indicating the robust bonding between PMS and catalyst. Besides, the intensities of Co-Fe-MDNI/PMS* increased over time (Fig. S17), manifesting the persistent binding of PMS to Co-Fe-MDNI. DFT calculations were also performed to calculate the adsorption energies of PMS on Co-MDNI, Fe-MDNI, and Co-Fe-MDNI. As shown in Fig. S18, all three structures exhibited excellent adsorption strength for PMS, further confirming the strong interaction between materials and PMS. While the adsorption energy of PMS on Co-Fe-MDNI was relatively lower than Co-MDNI and Fe-MDNI, which was conducive to the release of PMS for further activation. Moreover, the adsorption energies of BPA on different catalysts were computed to examine the impact of electronic coupling on pollutant adsorption. In Fig. 3d, BPA exhibited extraordinary adsorption energy on Co-Fe-MDNI (−22.10 eV) compared to Co-MDNI (−2.37 eV) and Fe-MDNI (−2.11 eV), implying the reinforced affinity between BPA and Co-Fe-MDNI. Therefore, by incorporating the analysis of the electronic structure and the experiment with different variables (Fig. S19–S22), the successful amalgamation of pollutants, catalysts, and PMS can be

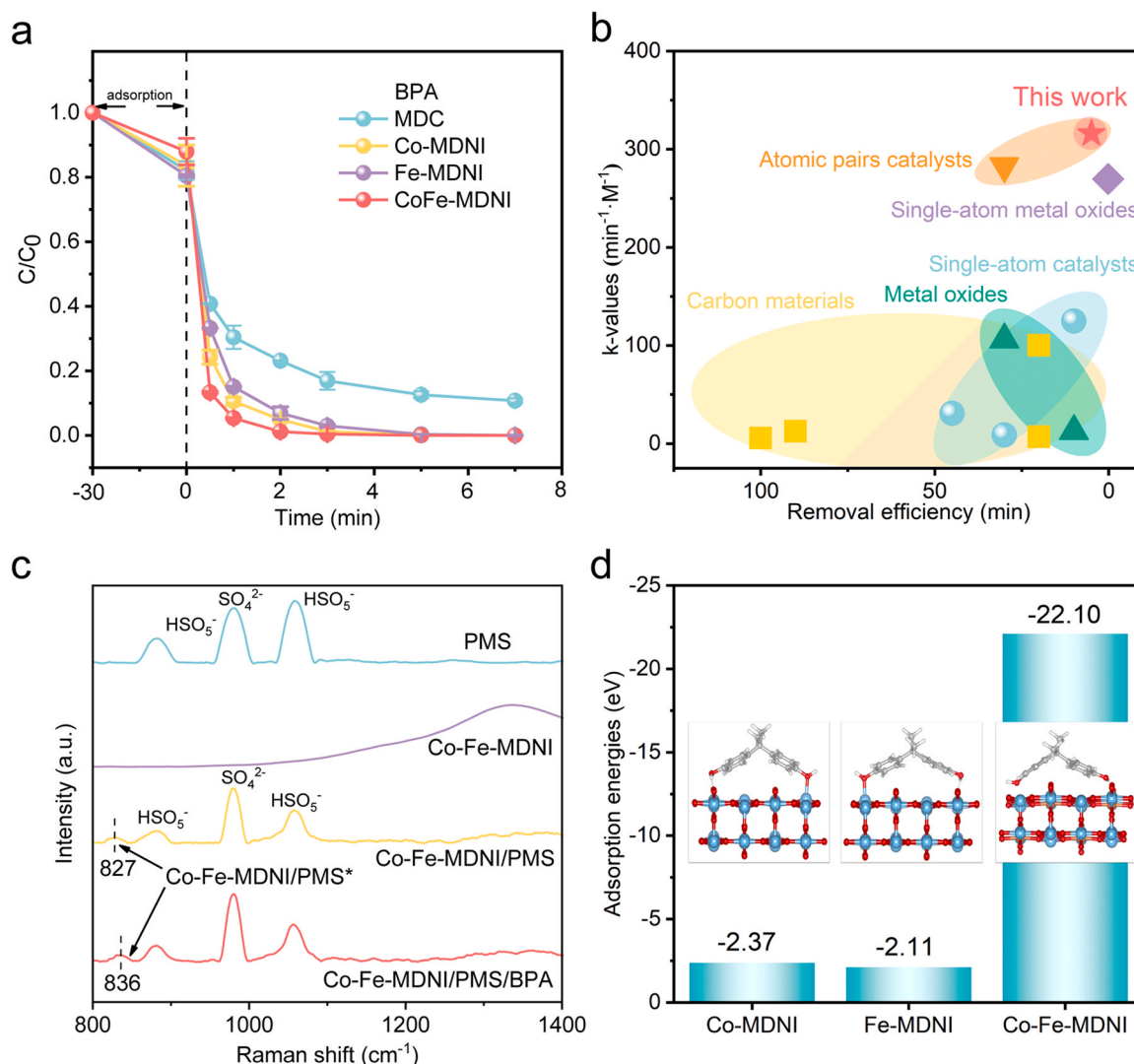


Fig. 3. a) The degradation curves of MDC, Co-MDNI, Fe-MDNI, and Co-Fe-MDNI for BPA. Experimental conditions: $[\text{Catalyst}]_0 = 0.1 \text{ g/L}$, $[\text{PMS}]_0 = 0.65 \text{ mM}$, $[\text{BPA}]_0 = 10 \text{ mg/L}$, $[\text{PBS}]_0 = 1 \text{ mM}$, $\text{pH} = 8.5$. b) Comparison of k -values of the advanced catalytic materials for BPA removal. c) In situ Raman spectra of different systems. d) The adsorption energies of PMS on Co-MDNI, Fe-MDNI, and Co-Fe-MDNI.

inferred. Additionally, the facilitation of seamless combination is partially attributed to the protruding nano-island structure, which brings Co-Fe-MDNI into closer proximity with PMS and pollutants, thereby effectively promoting the formation of ternary catalytic interfaces.

3.3. Establishment of electron transport channels

Based on ternary catalytic interfaces, the pathway of PMS activation for pollutants degradation was determined by quenching experiments (see supporting file for further details). As depicted in Fig. 4a, the degradation of BPA by MDC primarily depended on nonradical $^1\text{O}_2$ pathway and free radical pathway. In contrast, electron transfer, O_2 and $^1\text{O}_2$ were the main degradation pathways, among which electron transfer accounted for the highest proportion. The different dominant degradation pathways observed suggest that the Co-Fe atomic pairs facilitate the transition of pathway, leading to an increased degradation rate of BPA. Hence, the observed enhancement in k_{obs} of Co-Fe-MDNI can be attributed to the augmentation of the electron transfer pathway, where the initiation points (electrons extracted from pollutants) and termination points (electrons transported to PMS) of ETCs hold considerable significance.

The initiation points, where electron transport occurs between pollutants and catalysts, were investigated using electrochemical tests. As depicted in Fig. 4b, the open circuit potential and current value both exhibited a pronounced reduction upon the addition of BPA, reflecting that electron transport existed between the pollutant and Co-Fe-MDNI. In previous Fig. 3c, the addition of BPA into Co-Fe-MDNI/PMS* system resulted in a red shift of the Co-Fe-MDNI/PMS* peak, indicating the occurrence of electron transport between BPA and Co-Fe-MDNI/PMS*. This phenomenon was further substantiated by the notable peak shift from 814 cm^{-1} to 836 cm^{-1} observed in Fig. S23. Moreover, a remarkable linear correlation was observed between the single-electron oxidation potentials ($\phi_{1/2}$) and k_{obs} values of various pollutants, with an R^2 coefficient of up to 0.859 (Fig. 4c, Fig. S24–27, Table S7), which indicated the close relationship between the degradation rate of pollutants and the occurrence of electron transport at initiation points. Besides, the redox potentials of organic pollutants can be influenced by the pH of the solution, thereby affecting initiation points. As shown in Fig. 4d, BPA degradation was significantly inhibited at low pH due to the higher concentration of H^+ ions, which increased the reduction potential of pollutants and made BPA less likely to lose electrons to Co-Fe-MDNI/PMS*, diminishing the degradation rate from 2.06 min^{-1} to 1.13 min^{-1} . Conversely, a high concentration of OH^- ions reduced the

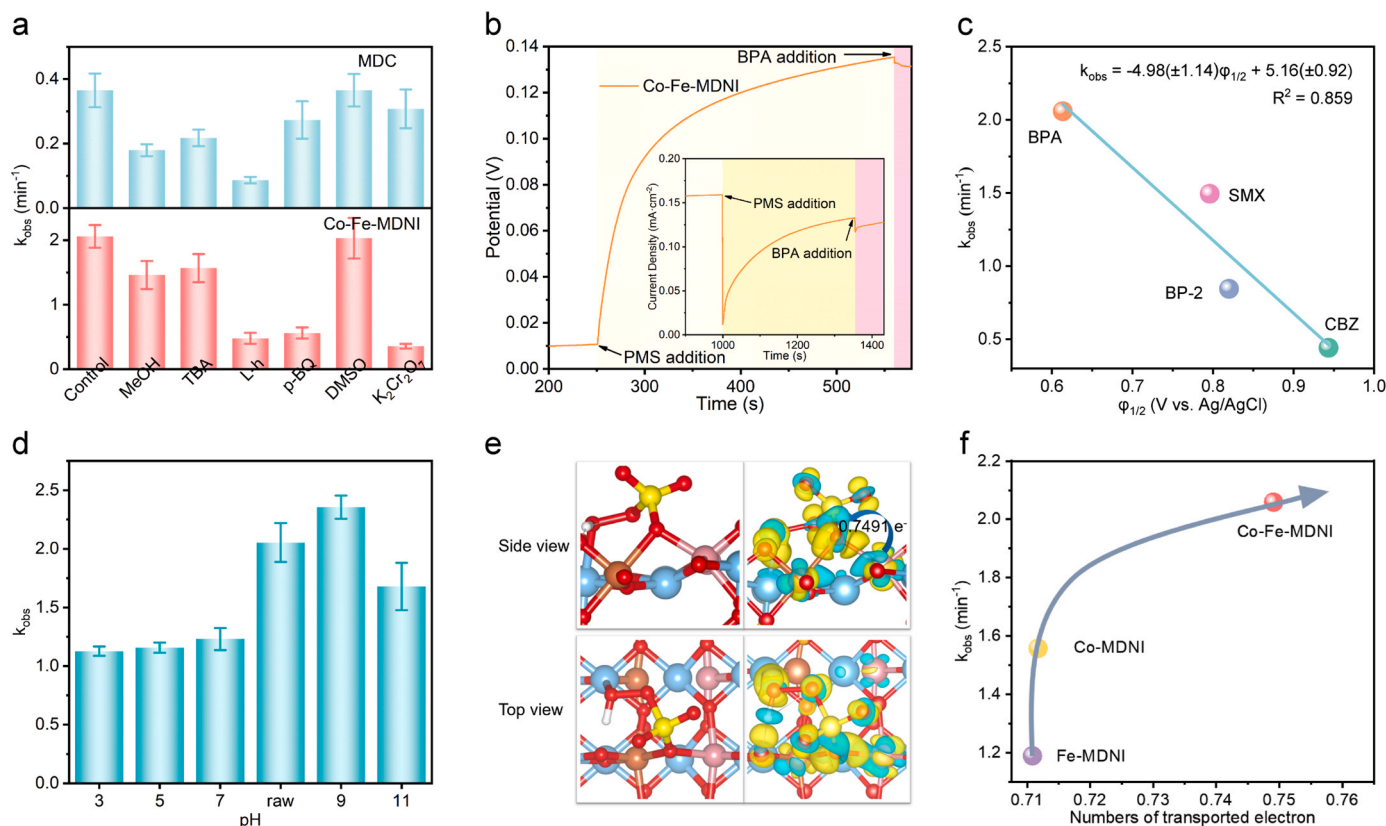


Fig. 4. a) The inhibitions of different quench agents on the degradation of BPA. b) The variations of potential and current in Co-Fe-MDNI/PMS* system. c) Correlation analysis between $\phi_{1/2}$ of different pollutants and corresponding k_{obs} . d) The effect of pH on BPA degradation by Co-Fe-MDNI. e) The electron transport between PMS and Co-Fe-MDNI. f) The relationship between electron transport and k_{obs} .

reduction potential of pollutants, while excessively high pH values were not conducive to PMS activation, resulting in a decrease in the pollutant removal rate. Moreover, the pH of initial pollutant solution was measured to be approximately 8.5, which signified a favorable electron transport efficiency. Accordingly, the efficacy of electron extraction from a specific pollutant predominantly relied on the electron-capture capability of catalyst. In this regard, the Co-Fe-MDNI demonstrated a pronounced augmentation in the process, suggesting a reduction of the energy barriers at initiation points, which might be ascribed to the distinctive electronic coupling feature of catalyst.

The investigation of termination points focused on the interaction between catalyst and PMS. As depicted in Fig. 4b, the PMS addition elevated the voltage and lowered the current, affirming the occurrence of electron transport between Co-Fe-MDNI and PMS. The extent of electron transport varied among the surface-confined complexes formed between PMS and Co-MDNI, Fe-MDNI, and Co-Fe-MDNI, as revealed by DFT calculations (Fig. 4e). The total electron transport from Co and Fe sites to PMS was highest for Co-Fe-MDNI (0.750 e) compared to Co-MDNI (0.712 e) and Fe-MDNI (0.711 e), as shown in Table S8, which could result in stronger electronic interaction within the Co-Fe-MDNI/PMS*. Remarkably, a relationship was observed between the k_{obs} values for Co-MDNI, Fe-MDNI, and Co-Fe-MDNI against the calculated number of transported electrons (Fig. 4f), suggesting that a higher number of transported electrons corresponds to a lower energy barrier, which further boosted the activation of PMS and thus expedited the degradation of pollutants. Comparatively, the energy barrier between Co-Fe-MDNI and PMS was lower than that of systems unable to form catalyst/PMS* composites [23]. Additionally, the presence of additional bonds between Co-Fe atomic pairs and PMS expanded the ETCs and effectively reduced the terminal energy barrier compared to single atom catalysts. Therefore, Co-Fe-MDNI adeptly reduced the energy barriers of

the initiation and termination points, rendering the ETCs more proficient and streamlined. Nevertheless, the underlying mechanism by which the electronic structure, particularly the modulation of d-orbitals as mention above, orchestrates the regulation of energy barriers remained inadequately elucidated.

3.4. Two-step energy barriers associated with d-orbitals

To elucidate the alteration of d-orbitals in Co-Fe-MDNI, the projected state densities (PDOS) of optimized models were calculated. As evidenced in Fig. 6a–b and S28–S29, the PDOS displayed an asymmetric distribution of each d-orbital electrons in both spin directions of Co-MDNI, Fe-MDNI, and Co-Fe-MDNI, suggesting different degrees of spin polarization. Notably, the PDOS of Co-Fe-MDNI exhibited significantly stronger spin polarization, consistent with the calculated magnetic moments, as revealed by the ELF and electronic spin density distributions mentioned before. The observed enhancement in spin polarization can be attributed to the reordering of d-orbital energy levels, as deduced from a comprehensive analysis of orbital occupancy and energy levels utilizing crystal field theory. Changes in the energy levels of electron orbits can induce electron migration, leading to alterations in the number of unpaired electrons within the orbitals, consequently affecting the electron spin state. As the electron spin state intensifies, with all electron spin directions aligned, a spin-polarized state becomes evident. Thus, the centers of five different d-orbitals for MDC and Co-Fe-MDNI were calculated, and the results are presented in Table S9. The data revealed that the d-orbitals of MDC were split into five distinct states, including d_{xy}^2 , d_{yz}^2 , d_{xz}/d_{yz} (double degenerate), and d_{xy} states. The splitting energy between highest and lowest orbital energy levels could be calculated to be 0.4458 eV. In the case of Co-Fe-MDNI, the electronic coupling led to an increase in the energy level of d_{yz}^2 orbital, forming the

double degenerate e_g orbital consisting of d_z^2 and d_{xy}^2 orbitals. Consequently, some electrons from the elevated d_z^2 orbital spilled over into the d_{xz}/d_{yz} orbitals, increasing the unpaired electron numbers. As a result, the d_{xz}/d_{yz} orbital energy level dropped, forming a triple degenerate state (d_{xz} , d_{yz} , and d_{xy}) with t_{2g} symmetry. The evaluated splitting energy of Co-Fe-MDNI (0.1221 eV) was lower than that of MDC, implying the d -orbital levels were changed by electronic coupling, which affected the numbers of unpaired electrons and d -orbital unoccupancy.

The augmentation of unpaired electrons in the LUCO (lowest unoccupied crystal orbital) conferred a favorable capacity for electron capture from pollutants, leading to a reduction in the energy barrier I (initiation points) as shown in Fig. 5. Conversely, the escalation in electrons in the HOCO (highest occupied crystal orbital) bolstered electron release to the PMS, thereby effectively lowering the energy barrier II (termination points). To quantify the two-step energy barriers, the HOMO (highest occupied molecular orbital) of BPA and LUMO (lowest unoccupied molecular orbital) of PMS were calculated, as well as the LUCO and HOCO of Fe-MDNI, Co-MDNI, and Co-Fe-MDNI were determined based on the band edge positions of d_{xz}/d_{yz} and d_z^2 orbitals (Table S10). Consequently, the energy barriers I ($BPA_{HOMO} \rightarrow Catalyst_{LUCO}$) and the energy barriers II ($Catalyst_{HOCO} \rightarrow PMS_{LUMO}$) were calculated to obtain the two-step energy barrier sums for Fe-MDNI (6.50 eV), Co-MDNI (5.84 eV), and Co-Fe-MDNI (4.83 eV). Through the analysis of two-step energy barriers and their comparison with the k_{obs} values of the three materials, a strong correlation with a high coefficient of 0.999 was observed in Fig. 6c. The observed correlation highlights the significant effect of electronic coupling, which effectively elevates the d -orbital unoccupancy and reduces the two-step energy barriers. More importantly, the reduction in energy barriers is directly associated with the enhanced rate of pollutant removal, underscoring the critical role of electron transport in the PMS activation by Co-Fe-MDNI.

3.5. Effect of electronic coupling on two-step energy barriers

To analyze the orbital interactions and quantify the effect of electronic coupling on the energy barriers, a crystal orbital Hamiltonian population (COHP) analysis was performed. Specifically, the electronic coupling can affect the interaction between electrons in d -orbitals of the active metals and p -orbitals of coordinated O in Co-MDNI, Fe-MDNI, and Co-Fe-MDNI [46]. To investigate the distinct bonding states of the five d -orbitals (d_{xy}^2 , d_z^2 , d_{xz} , d_{yz} , and d_{xy}) of Co-MDNI, Fe-MDNI, and

Co-Fe-MDNI, a projection COHP (pCOHP) analysis was conducted. As depicted in Fig. 6d–f, the number of antibonding orbitals occupied by electrons below the Fermi level exceeded that of the bonding orbitals in Co-MDNI and Fe-MDNI, whereas the situation was precisely opposite in Co-Fe-MDNI. Comparing Fig. 6d and f, it was observed that the occupancy of anti-bonding orbitals of d_{xz}/d_{yz} and d_z^2 in Co-MDNI was relatively higher, whereas in Co-Fe-MDNI, the d_{xy} and d_z^2 orbitals dominated and the overall electron occupancy decreases significantly in the anti-bonding orbitals. Similarly, comparing Fig. 6e and f, electrons occupied the anti-bonding orbitals of d_{xz}/d_{yz} and d_z^2 in Fe-O of Fe-MDNI, whereas the anti-bonding orbitals of Co-Fe-MDNI were almost unoccupied. Notably, the d_{xz}/d_{yz} and d_z^2 bonding orbitals exhibited a conspicuous electron occupation in Co-Fe-MDNI compared with other two configurations. These findings reflected the alterations in bonding orbitals of the active metals and confirmed that the d -orbital splitting behavior was modified as a consequence of electronic coupling, which led to a notable reduction in the energy levels of d_{xz}/d_{yz} and elevation of d_z^2 orbitals, accompanied by an enhanced electron occupancy. Furthermore, the COHP calculations revealed that Co-Fe-MDNI exhibited a higher integral value of the bonding state (ICOHP) below the Fermi level, which could be attributed to the robust electronic coupling of Co-Fe atomic pairs. The values of ICOHP in d_{xz}/d_{yz} and d_z^2 orbitals, as well as two-step energy barriers and k_{obs} for the three catalysts, are provided in Table S11. To quantitatively assess the impact of electron coupling on the energy barriers, linear regression analysis was conducted to determine the correlation between the ICOHP and the two-step energy barrier sums of three configurations. The obtained R^2 correlations reached a high value of 0.923, providing strong evidence for the ability of electronic coupling to effectively reduce the two-step energy barriers (Fig. 6c). By combining the correlation analysis between the previously determined two-step energy barrier and k_{obs} , it became evident that the ICOHP value was also associated with k_{obs} (Fig. S30). The correlation among the three factors (ICOHP, energy barrier, and k_{obs}) highlighted the potential of orbital interactions, quantified by ICOHP, to serve as a descriptor for the degradation rate of pollutants through electron-mediated PMS activation, via the association of two-step energy barriers. In a word, the physical and electronic structure of Co-Fe atomic paired nano-islands facilitated the formation of ternary catalytic interfaces. Furthermore, the electronic coupling between Co-Fe atomic pairs, quantifiable by ICOHP, significantly lowered the two-step energy barriers and expanded the ETCs. This allowed for the efficient transfer of electrons from pollutants to the catalyst and subsequently to

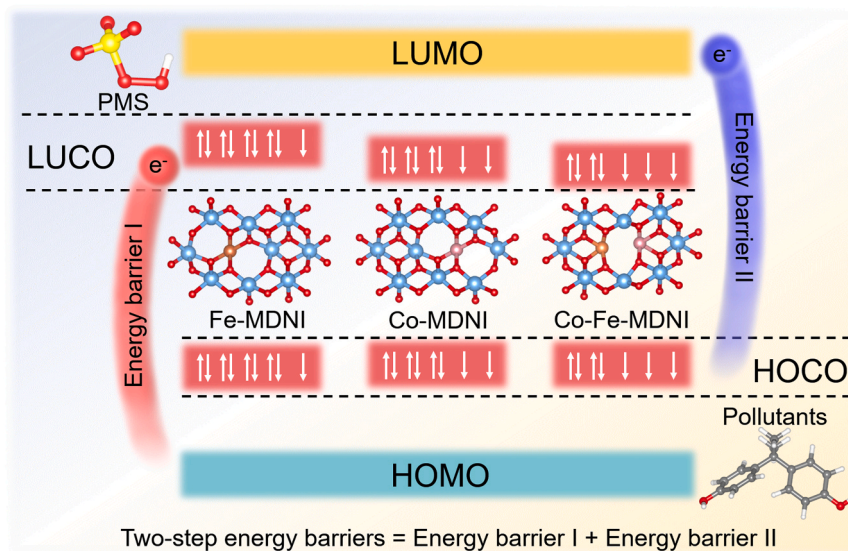


Fig. 5. The two-step energy barriers for electron transport over catalysts.

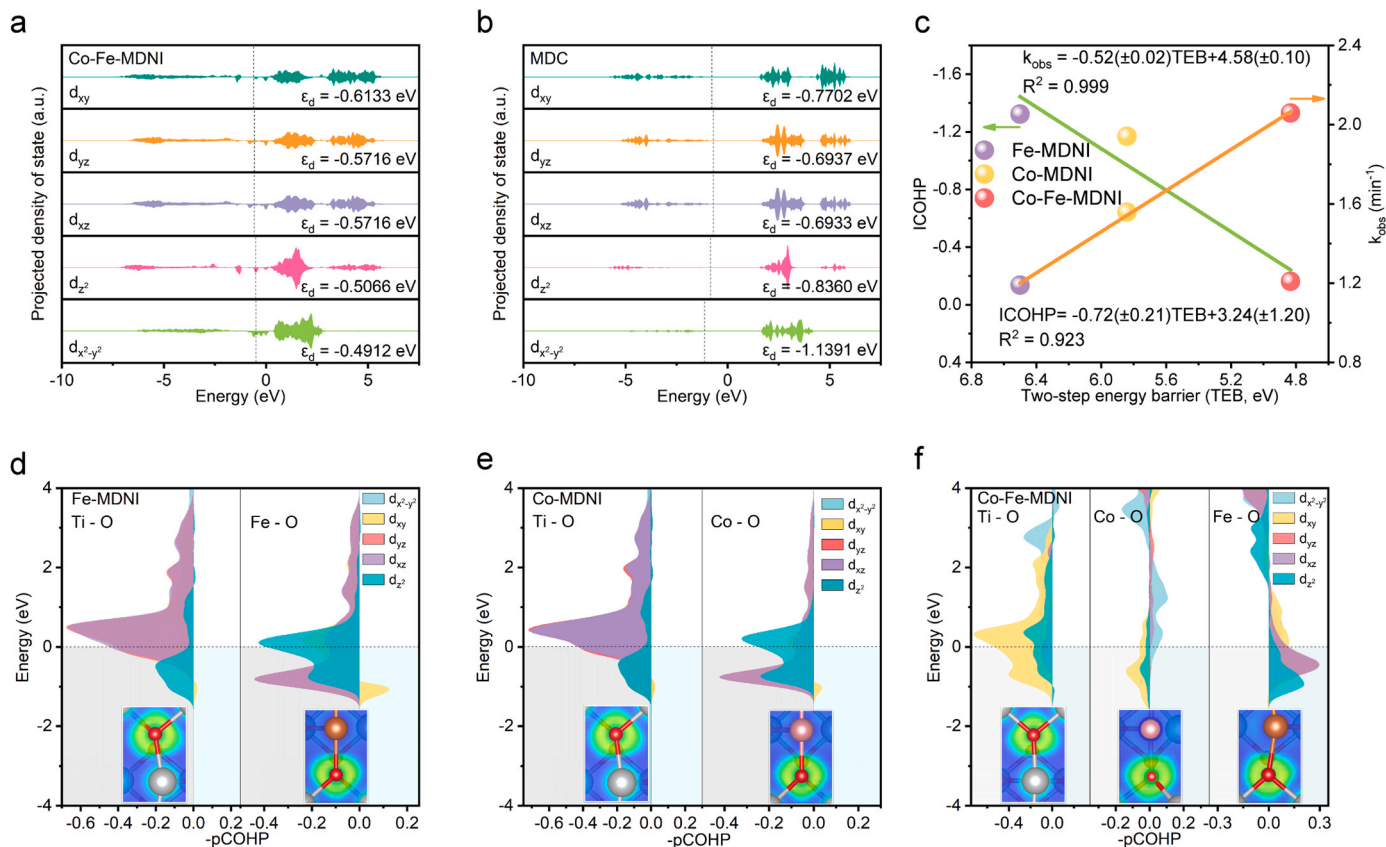
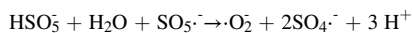
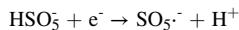


Fig. 6. The PDOS of a) Co-Fe-MDNI and b) MDC. c) The correlation analysis of two-step energy barriers, ICOHP, and k_{obs} . The pCOHP of d) Co-MDNI, e) Fe-MDNI, and f) Co-Fe-MDNI.

PMS, thereby completing the electron-mediated PMS activation process. This finding indicates the interconnectivity between surface-interface reactions and electronic structures, transcending the boundaries across macroscopic to microscopic scales, shedding light on the regulation of electron-orbital interactions to enhance the catalytic activity, which in turn provides clear guidance on the optimization of two-step energy barriers for electron-mediated PMS activation systems.

3.6. Impact of transition of BPA degradation pathways

After electrons were transported to PMS, the generation of $\cdot\text{O}_2^-$ and negligible $^1\text{O}_2$ was confirmed through EPR analysis (Fig. 7a). As $\cdot\text{O}_2^-$ is a very weak oxidant, which could be viewed as $\cdot\text{OH}$ source, and in this way $\cdot\text{O}_2^-$ was likely to contribute to degradation. Consequently, the equations for the formation of $\cdot\text{O}_2^-$ were shown as follows:



To gain a better understanding of the detailed degradation process, the Fukui indices and LC-MS were performed to reveal the reactive sites and possible degradation pathways of BPA over Co-Fe-MDNI. LC-MS was employed to detect the intermediate products of degraded BPA over Co-Fe-MDNI and MDC. The degraded BPA solution showed different LC-MS signals at $m/z = 290, 280, 244, 228, 174, 146, 123$ and 94 , as displayed in Fig. S31–S32. Based on the results of LC-MS and Fukui indices (Fig. S33, Table S12) [47–49], three possible reaction pathways of BPA degradation were identified (Fig. 7b). Considering the natural occurrence of BPA at low concentrations, bioconcentration factor was employed as an indicator to evaluate the risks of the intermediate products in three distinct degradation pathways using Toxicity Estimation Software Tool (T.E.S.T.). As illustrated in Fig. 7c, the degradation intermediates in

pathway I (electron transfer) were found to be the least toxic, with a toxicity area value of 12.546. In contrast, intermediate products in pathway II ($^1\text{O}_2$) and pathway III (free radical) exhibited higher toxicity area values of 13.961 and 32.842, respectively, which suggested that intermediates originating from these two pathways have a higher potential for human toxicity due to their propensity for accumulation (Fig. S34). In view of that the MDC predominantly activated PMS to degrade pollutants via $^1\text{O}_2$ and free radical pathways, whereas Co-Fe-MDNI primarily operated through electron transfer pathway. The different dominant pathways suggest that the reduction of two-step energy barriers achieved by electronic coupling facilitates a transition in the degradation pathway and mitigates the ecological risks associated with the bioaccumulation of pollutant intermediates. Furthermore, after four cycles, the BPA removal efficiency consistently exceeded 90 % as depicted in Fig. S35, indicating remarkable stability.

4. Conclusion

In summary, a nano-island structure with Co-Fe atomic pairs was constructed to expedite the electron transfer pathway. Leveraging the structural advantages of nano-islands, PMS and pollutants exhibited a greater affinity for the exposed active sites on Co-Fe-MDNI, leading to the formation of ternary catalytic interfaces and facilitating PMS activation. Furthermore, the electronic coupling of Co-Fe atomic pairs induced changes in the splitting behavior of d-orbitals and elevated the d-orbital unoccupancy, punching through the ETCs. The reduction of two-step energy barriers ultimately improved the intrinsic activity of the catalyst and expedited the electron transfer pathway. Consequently, Co-Fe-MDNI exhibited an exceptional degradation rate of 2.06 min^{-1} for BPA degradation via electron-mediated PMS activation. Notably, the transition of degradation pathway into electron transfer reduced the

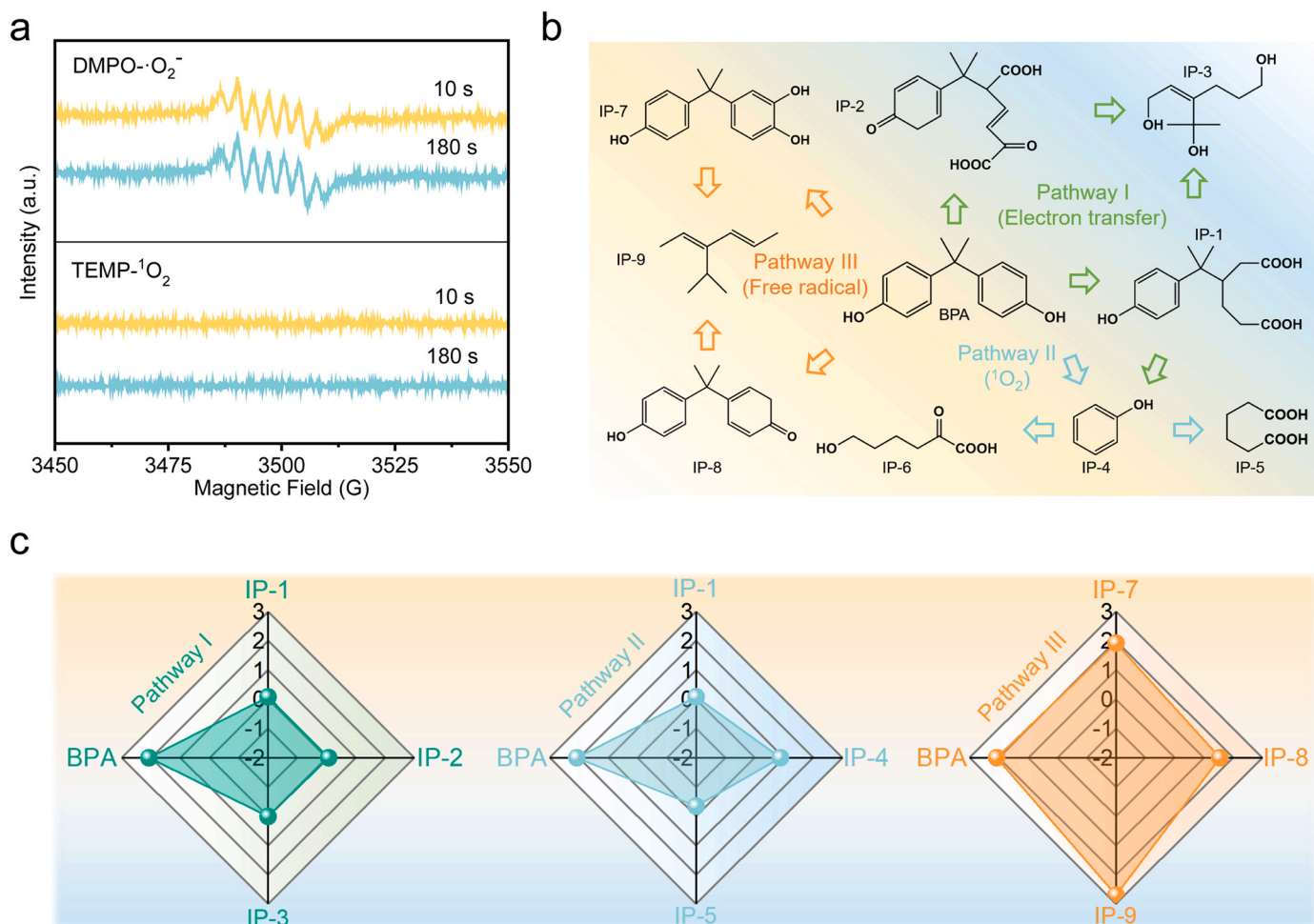


Fig. 7. a) EPR spectra of Co-Fe-MDNI for DMPO- $\cdot\text{O}_2^-$ and TEMP- $^1\text{O}_2$. b) The possible degradation pathways of BPA by Co-Fe-MDNI. c) The bioaccumulation risks of intermediates in different degradation pathways.

bioaccumulation risks of intermediate products compared to other pathways. This work not only offers an efficient approach for developing highly effective catalysts but also offers valuable atomic-level insights into electron-mediated reactions and metal center modulation.

CRedit authorship contribution statement

Junjie Xu: Writing-Original draft preparation, Methodology, Software. **Yanchi Yao:** Data curation, Conceptualization. **Chao Zhu:** Visualization, Investigation. **Lun Lu:** Software, Validation. **Qile Fang:** Software, Validation. **Zhiqiao He:** Writing – Reviewing and Editing. **Shuang Song:** Supervision. **Baoliang Chen:** Writing – Reviewing and Editing. **Yi Shen:** Writing – Reviewing and Editing, Supervision.

Declaration of Competing Interest

The authors declare that they have no known competing financial interests or personal relationships that could have appeared to influence the work reported in this paper.

Data Availability

Data will be made available on request.

Acknowledgments

This research was supported by the National Natural Science

Foundation of China (22276171, 22006131, 22106136), the Fundamental Research Funds for the Provincial Universities of Zhejiang (RF-C2023009), the China Postdoctoral Science Foundation (2022M722811, 2020T130598, 2019M662106), the Zhejiang Provincial Natural Science Foundation of China (LQ20B070010), Zhuhai Science and Technology Bureau (ZH22017003210025PWC).

Appendix A. Supporting information

Supplementary data associated with this article can be found in the online version at [doi:10.1016/j.apcatb.2023.123356](https://doi.org/10.1016/j.apcatb.2023.123356).

References

- [1] C. Chen, C. Ma, Y. Yang, X. Yang, K. Demeestere, A. Nikiforov, S. Van Hulle, Degradation of micropollutants in secondary wastewater effluent using nonthermal plasma-based AOPs: the roles of free radicals and molecular oxidants, *Water Res.* 235 (2023), 119881, <https://doi.org/10.1016/j.watres.2023.119881>.
- [2] Y. Shen, C. Zhu, S. Song, T. Zeng, L. Li, Z. Cai, Defect-abundant covalent triazine frameworks as sunlight-driven self-cleaning adsorbents for volatile aromatic pollutants in water, *Environ. Sci. Technol.* 53 (2019) 9091–9101, <https://doi.org/10.1021/acs.est.9b02222>.
- [3] D. Wang, Y. He, Y. Chen, F. Yang, Z. He, T. Zeng, X. Lu, L. Wang, S. Song, J. Ma, Electron transfer enhancing the Mn(II)/Mn(III) cycle in MnO/CN towards catalytic ozonation of atrazine via a synergistic effect between MnO and CN, *Water Res.* 230 (2023), 119574, <https://doi.org/10.1016/j.watres.2023.119574>.
- [4] Y. Shen, J. Hu, L. Lu, C. Zhu, Q. Fang, S. Song, Enhanced photocatalytic performance of S-doped covalent triazine framework for organic pollutant degradation, *J. Zhejiang Univ. Sci. A* 23 (2022) 988–997, <https://doi.org/10.1631/2023.A2200440>.

- [5] Y. Gao, T. Wu, C. Yang, C. Ma, Z. Zhao, Z. Wu, S. Cao, W. Geng, Y. Wang, Y. Yao, Y. Zhang, C. Cheng, Activity trends and mechanisms in peroxymonosulfate-assisted catalytic production of singlet oxygen over atomic metal-N-C catalysts, *Angew. Chem. Int. Ed.* 60 (2021) 22513–22521, <https://doi.org/10.1002/anie.202109530>.
- [6] K. Yin, Y. Shang, D. Chen, B. Gao, Q. Yue, X. Xu, Redox potentials of pollutants determining the dominate oxidation pathways in manganese single-atom catalyst (Mn-SAC)/peroxymonosulfate system: selective catalytic mechanisms for versatile pollutants, *Appl. Catal. B Environ.* 338 (2023), 123029, <https://doi.org/10.1016/j.apcatb.2023.123029>.
- [7] Y. Shang, Y. Kan, X. Xu, Stability and regeneration of metal catalytic sites with different sizes in Fenton-like system, *Chin. Chem. Lett.* 34 (2023), 108278, <https://doi.org/10.1016/j.ccllet.2023.108278>.
- [8] K.Z. Huang, H. Zhang, Direct electron-transfer-based peroxymonosulfate activation by iron-doped manganese oxide (δ -MnO₂) and the development of galvanic oxidation processes (GOPs), *Environ. Sci. Technol.* 53 (2019) 12610–12620, <https://doi.org/10.1021/acs.est.9b03648>.
- [9] K. Yin, L. Peng, D. Chen, S. Liu, Y. Zhang, B. Gao, K. Fu, Y. Shang, X. Xu, High-loading of well dispersed single-atom catalysts derived from Fe-rich marine algae for boosting Fenton-like reaction: role identification of iron center and catalytic mechanisms, *Appl. Catal. B Environ.* 336 (2023), 122951, <https://doi.org/10.1016/j.apcatb.2023.122951>.
- [10] J. Yu, L. Tang, Y. Pang, X. Liang, Y. Lu, H. Feng, J. Wang, L. Deng, J. Zou, X. Zhu, J. Tang, Non-radical oxidation in environmental catalysis: recognition, identification, and perspectives, *Chem. Eng. J.* 433 (2022), 134385, <https://doi.org/10.1016/j.cej.2021.134385>.
- [11] M. Yang, Z. Hou, X. Zhang, B. Gao, Y. Li, Y. Shang, Q. Yue, X. Duan, X. Xu, Unveiling the origins of selective oxidation in single-atom catalysis via Co–N₄–C intensified radical and nonradical pathways, *Environ. Sci. Technol.* 56 (2022) 11635–11645, <https://doi.org/10.1021/acs.est.2c01261>.
- [12] B.C. Hodges, E.L. Cates, J.-H. Kim, Challenges and prospects of advanced oxidation water treatment processes using catalytic nanomaterials, *Nat. Nanotechnol.* 13 (2018) 642–650, <https://doi.org/10.1038/s41565-018-0216-x>.
- [13] J. Xu, C. Zhu, S. Song, Q. Fang, J. Zhao, Y. Shen, A nanocubicle-like 3D adsorbent fabricated by in situ growth of 2D heterostructures for removal of aromatic contaminants in water, *J. Hazard. Mater.* 423 (2022), 127004, <https://doi.org/10.1016/j.jhazmat.2021.127004>.
- [14] K. Yin, R. Wu, Y. Shang, D. Chen, Z. Wu, X. Wang, B. Gao, X. Xu, Microenvironment modulation of cobalt single-atom catalysts for boosting both radical oxidation and electron-transfer process in Fenton-like system, *Appl. Catal. B Environ.* 329 (2023), 122558, <https://doi.org/10.1016/j.apcatb.2023.122558>.
- [15] Z. Li, B. Li, Q. Li, Single-atom nano-islands (SANIs): a robust atomic–nano system for versatile heterogeneous catalysis applications, *Adv. Mater.* 35 (2023) 2211103, <https://doi.org/10.1002/adma.202211103>.
- [16] A. Corma, H. García, Lewis acids as catalysts in oxidation reactions: from homogeneous to heterogeneous systems, *Chem. Rev.* 102 (2002) 3837–3892, <https://doi.org/10.1021/cr010333u>.
- [17] C. Zhu, L. Lu, J. Xu, S. Song, Q. Fang, R. Liu, Y. Shen, J. Zhao, W. Dong, Y. Shen, Metal monovacancy-induced spin polarization for simultaneous energy recovery and wastewater purification, *Chem. Eng. J.* 451 (2023), 138537, <https://doi.org/10.1016/j.cej.2022.138537>.
- [18] Y. Jiang, D. Baimanov, S. Jin, J. Cheuk-Fung Law, P. Zhao, J. Tang, J. Peng, L. Wang, K.S.-Y. Leung, W. Sheng, S. Lin, In situ turning defects of exfoliated Ti₃C₂ MXene into Fenton-like catalytic active sites, *Proc. Natl. Acad. Sci. U. S. A.* 120 (2023), e2210211120, <https://doi.org/10.1073/pnas.2210211120>.
- [19] L. Hui, X. Zhang, Y. Xue, X. Chen, Y. Fang, C. Xing, Y. Liu, X. Zheng, Y. Du, C. Zhang, F. He, Y. Li, Highly dispersed platinum chlorine atoms anchored on gold quantum dots for a highly efficient electrocatalyst, *J. Am. Chem. Soc.* 144 (2022) 1921–1928, <https://doi.org/10.1021/jacs.1c12310>.
- [20] R. Gao, J. Xu, J. Wang, J. Lim, C. Peng, L. Pan, X. Zhang, H. Yang, J.-J. Zou, Pd/Fe₂O₃ with electronic coupling single-site Pd–Fe pair sites for low-temperature semihydrogenation of alkynes, *J. Am. Chem. Soc.* 144 (2022) 573–581, <https://doi.org/10.1021/jacs.1c11740>.
- [21] Y. Bo, H. Wang, Y. Lin, T. Yang, R. Ye, Y. Li, C. Hu, P. Du, Y. Hu, Z. Liu, R. Long, C. Gao, B. Ye, L. Song, X. Wu, Y. Xiong, Altering hydrogenation pathways in photocatalytic nitrogen fixation by tuning local electronic structure of oxygen vacancy with dopant, *Angew. Chem. Int. Ed.* 60 (2021) 16085–16092, <https://doi.org/10.1002/anie.202104001>.
- [22] Z. Zhou, M. Li, Y. Zhang, L. Kong, V.F. Smith, M. Zhang, A.J. Gulbrandson, G. H. Waller, F. Lin, X. Liu, D.P. Durkin, H. Chen, D. Shuai, Fe–Fe double-atom catalysts for murine coronavirus disinfection: nonradical activation of peroxides and mechanisms of virus inactivation, *Environ. Sci. Technol.* 57 (2023) 3804–3816, <https://doi.org/10.1021/acs.est.3c00163>.
- [23] B. Wang, C. Cheng, M. Jin, J. He, H. Zhang, W. Ren, J. Li, D. Wang, Y. Li, A site distance effect induced by reactant molecule matchup in single-atom catalysts for Fenton-like reactions, *Angew. Chem. Int. Ed.* 61 (2022), e202207268, <https://doi.org/10.1002/anie.202207268>.
- [24] C. Zhu, L. Lu, Q. Fang, S. Song, B. Chen, Y. Shen, Unveiling spin state-dependent micropollutant removal using single-atom covalent triazine framework, *Adv. Funct. Mater.* 33 (2023) 2210905, <https://doi.org/10.1002/adfm.202210905>.
- [25] Y. Shen, H. Zhang, B. Chen, C. Zhu, W. Yu, J. Yang, Q. Fang, Z. He, T. Sun, S. Song, Mechanistic insight into electron orientation by tailoring Ni–Cu atom-pairs for high-performance CO₂ electroreduction, *Appl. Catal. B Environ.* 330 (2023), 122654, <https://doi.org/10.1016/j.apcatb.2023.122654>.
- [26] Y. Shen, S. Liu, L. Lu, C. Zhu, Q. Fang, R. Liu, Y. Shen, S. Song, Pyridine-linked covalent triazine frameworks with bidirectional electron donor-acceptor for efficient organic pollution removal, *J. Hazard. Mater.* 444 (2023), 130428, <https://doi.org/10.1016/j.jhazmat.2022.130428>.
- [27] Z. Kong, L. Lu, C. Zhu, J. Xu, Q. Fang, R. Liu, Y. Shen, Enhanced adsorption and photocatalytic removal of PFOA from water by F-functionalized MOF with in-situ-growth TiO₂: regulation of electron density and bandgap, *Sep. Purif. Technol.* 297 (2022), 121449, <https://doi.org/10.1016/j.seppur.2022.121449>.
- [28] S. Liu, L. Lu, C. Zhu, Q. Fang, S. Song, Y. Zheng, Y. Shen, The role of dual vacancies in TiO₂ for enhanced photocatalytic hydrogen generation and pollutants removal, *ChemCatChem* 14 (2022), e202201107, <https://doi.org/10.1002/cctc.202201107>.
- [29] Y. Shen, S. Liu, L. Lu, C. Zhu, Q. Fang, R. Liu, Z. He, Y. Li, S. Song, Photocatalytic degradation of toluene by a TiO₂ p–n homojunction nanostructure, *ACS Appl. Nano Mater.* 5 (2022) 18612–18621, <https://doi.org/10.1021/acsnano.2c04397>.
- [30] Y. Ma, X. Yi, S. Wang, T. Li, B. Tan, C. Chen, T. Majima, E.R. Wacławik, H. Zhu, J. Wang, Selective photocatalytic CO₂ reduction in aerobic environment by microporous Pd-porphyrin-based polymers coated hollow TiO₂, *Nat. Commun.* 13 (2022) 1400, <https://doi.org/10.1038/s41467-022-29102-0>.
- [31] S. Sarkar, A. Biswas, E.E. Siddharthan, R. Thapa, R.S. Dey, Strategic modulation of target-specific isolated Fe,Co single-atom active sites for oxygen electrocatalysis impacting high power Zn–air battery, *ACS Nano* 16 (2022) 7890–7903, <https://doi.org/10.1021/acsnano.2c00547>.
- [32] Y. Shen, Y. Yao, L. Lu, C. Zhu, Q. Fang, J. Wang, S. Song, Insights into dual effect of missing linker-cluster domain defects for photocatalytic 2e[−] ORR: radical reaction and electron behavior, *Chemosphere* 324 (2023), 138220, <https://doi.org/10.1016/j.chemosphere.2023.138220>.
- [33] J. Xu, C. Zhu, R. Liu, Q. Fang, Y. Zheng, Z. He, S. Song, Y. Shen, Elucidating the charge redistribution in bimetallic metal–organic frameworks: high-electron-density reactive center for removal of organic micropollutants in water, *Chem. Eng. J.* 468 (2023), 143723, <https://doi.org/10.1016/j.cej.2023.143723>.
- [34] B. Toby, EXPGUI, a graphical user interface for GSAS, *J. Appl. Crystallogr.* 34 (2001) 210–213, <https://doi.org/10.1107/S0021889801002242>.
- [35] Y. Fu, M. Tan, Z. Guo, D. Hao, Y. Xu, C. Zhang, J. Guo, Q. Li, Q. Wang, Fabrication of wide-spectra-responsive NA/NH₂-MIL-125(Ti) with boosted activity for Cr(VI) reduction and antibacterial effects, *Chem. Eng. J.* 452 (2023), 139417, <https://doi.org/10.1016/j.cej.2022.139417>.
- [36] Y. Shen, J. Wu, C. Zhu, J. Zhao, Q. Fang, Y. Zheng, C.T.J. Ferguson, S. Song, Bifunctional covalent triazine frameworks based on Ti–ON bonds for micropollutants removal: effects of 3D extended structure and electron transport bridges, *Chem. Eng. J.* 465 (2023), 143026, <https://doi.org/10.1016/j.cej.2023.143026>.
- [37] Y. Fu, K. Zhang, Y. Zhang, Y. Cong, Q. Wang, Fabrication of visible-light-active MR/NH₂-MIL-125(Ti) homojunction with boosted photocatalytic performance, *Chem. Eng. J.* 412 (2021), 128722, <https://doi.org/10.1016/j.cej.2021.128722>.
- [38] H. Tian, H. Tian, S. Wang, S. Chen, F. Zhang, L. Song, H. Liu, J. Liu, G. Wang, High-power lithium–selenium batteries enabled by atomic cobalt electrocatalyst in hollow carbon cathode, *Nat. Commun.* 11 (2020) 5025, <https://doi.org/10.1038/s41467-020-18820-y>.
- [39] Y. Li, S. Lin, D. Wang, T. Gao, J. Song, P. Zhou, Z. Xu, Z. Yang, N. Xiao, S. Guo, Single atom array mimic on ultrathin MOF nanosheets boosts the safety and life of lithium–sulfur batteries, *Adv. Mater.* 32 (2020) 1906722, <https://doi.org/10.1002/adma.201906722>.
- [40] Z. Fan, R. Luo, Y. Zhang, B. Zhang, P. Zhai, Y. Zhang, C. Wang, J. Gao, W. Zhou, L. Sun, J. Hou, Oxygen-bridged indium–nickel tomic pair as dual-metal active sites enabling synergistic electrocatalytic CO₂ reduction, *Angew. Chem. Int. Ed.* 62 (2023), e202216326, <https://doi.org/10.1002/anie.202216326>.
- [41] K. Chen, K. Liu, P. An, H. Li, Y. Lin, J. Hu, C. Jia, J. Fu, H. Li, H. Liu, Z. Lin, W. Li, J. Li, Y.-R. Lu, T.-S. Chan, N. Zhang, M. Liu, Iron phthalocyanine with coordination induced electronic localization to boost oxygen reduction reaction, *Nat. Commun.* 11 (2020) 4173, <https://doi.org/10.1038/s41467-020-18062-y>.
- [42] L. Huang, D. Chen, G. Luo, Y.-R. Lu, C. Chen, Y. Zou, C.-L. Dong, Y. Li, S. Wang, Zirconium-regulation-induced bifunctionality in 3D cobalt–iron oxide nanosheets for overall water splitting, *Adv. Mater.* 31 (2019) 1901439, <https://doi.org/10.1002/adma.201901439>.
- [43] R. Lin, L. Kang, K. Lisowska, W. He, S. Zhao, S. Hayama, G.J. Hutchings, D.J. L. Brett, F. Corà, I.P. Parkin, G. He, Approaching theoretical performances of electrocatalytic hydrogen peroxide generation by cobalt–nitrogen moieties, *Angew. Chem. Int. Ed.* 62 (2023), e202301433, <https://doi.org/10.1002/anie.202301433>.
- [44] H. Fei, J. Dong, Y. Feng, C.S. Allen, C. Wan, B. Voloskiy, M. Li, Z. Zhao, Y. Wang, H. Sun, P. An, W. Chen, Z. Guo, C. Lee, D. Chen, I. Shakir, M. Liu, T. Hu, Y. Li, A. I. Kirkland, X. Duan, Y. Huang, General synthesis and definitive structural identification of MN₄C₄ single-atom catalysts with tunable electrocatalytic activities, *Nat. Catal.* 1 (2018) 63–72, <https://doi.org/10.1038/s41929-017-0008-y>.
- [45] Y. Dai, B. Liu, Z. Zhang, P. Guo, C. Liu, Y. Zhang, L. Zhao, Z. Wang, Tailoring the d-orbital splitting manner of single atomic sites for enhanced oxygen reduction, *Adv. Mater.* 35 (2023) 2210757, <https://doi.org/10.1002/adma.202210757>.
- [46] J. Zhu, M. Xiao, D. Ren, R. Gao, X. Liu, Z. Zhang, D. Luo, W. Xing, D. Su, A. Yu, Z. Chen, Quasi-covalently coupled Ni–Cu atomic pair for synergistic electroreduction of CO₂, *J. Am. Chem. Soc.* 144 (2022) 9661–9671, <https://doi.org/10.1021/jacs.2c00937>.

- [47] T. Lu, F. Chen, Multiwfn: a multifunctional wavefunction analyzer, *J. Comput. Chem.* 33 (2012) 580–592, <https://doi.org/10.1002/jcc.22885>.
- [48] T. Lu, Q. Chen, Realization of conceptual density functional theory and information-theoretic approach in multiwfn program, in *Conceptual Density Functional Theory*. 2022. p. 631–647, <https://doi.org/10.1002/9783527829941.ch31>.
- [49] Y. Shen, J. Yang, C. Zhu, Q. Fang, S. Song, B. Chen, Mechanistic insights into the atomic distance effect on adsorption and degradation of aromatic compounds, *ACS Catal.* 13 (2023) 8943–8954, <https://doi.org/10.1021/acscatal.3c02095>.